MNE 31 (2026) 100357

Contents lists available at ScienceDirect

Micro and Nano Engineering

journal homepage: www.elsevier.com/locate/mne

Research paper

A 3D-printed contactless RF voltage and current probe for micrometre resolution inspection of integrated circuits

Maarten Jankie [a], Thomas Hackl [b], Georg Schitter [b], Urs Staufer [a,*]

[a] Department of Precision and Microsystems Engineering (PME), TU Delft, Mekelweg 2, Delft, 2628CD, South-Holland, The Netherlands
[b] Mechatronics and Power Electronics Institute (MPEI), TU Wien, Gusshausstrasse 27-29, Vienna, 1040, Vienna, Austria

ARTICLE INFO

Keywords:
Contactless model-based RF probing
Multi-functional electrical probe
Microfabricated pick-up coil
Multiscale 3D printing

ABSTRACT

As a result of current trends in miniaturisation and the need for faster electronic circuits, integrated circuit (IC) design has become more complex. Closely packed conductors carrying radiofrequency (RF) signals are subjected to parasitic coupling, complicating the IC design and validation. Prototyping of such devices is supported by contact probes that make an ohmic connection to contact pads. These pads take up valuable space and may interfere with the design. Alternatively, near-field probing techniques, that utilise capacitive and inductive coupling, have been employed for local RF voltage and current characterisation. In this research, such a near-field probe is developed through a multiscale 3D-printing process. It contains a miniaturised conductive loop, enclosing an area of 12.5 μm^2, and a conductive tip with an apex radius of 100 nm. A model-based approach, that makes use of the discrepancy between parasitic long-range, and local short-range contributions to the measurement signal, is expanded to conduct both RF voltage and current measurements with increased spatial resolution. With this approach, combined contactless RF-voltage and RF-current measurements were executed demonstrating a measurement bandwidth from 1 to 23 GHz. Capacitively coupled RF-voltage measurements achieved a spatial resolution of 8 μm, while the spatial resolution of inductively coupled current measurements was only simulated. The simulation shows an expected spatial resolution of 3 μm.

1. Introduction

The drive for faster devices has led to the rise of Radiofrequency Integrated Circuits (RFICs), which pose challenges in electromagnetic compatibility [1] as well as characterisation [2]. Conventional contact-based characterisation methods use radiofrequency (RF) contact probes, which require contact pads to connect to the Device Under Test (DUT) [3]. In the case of RFICs, features are often small compared to the contact pads, making it difficult to characterise local voltages and currents with μm-resolution. Parasitic coupling to surrounding features further complicates the local identification of voltages and currents, as contact measurements require a well-defined model between the measurement input and output [4]. Alternatively, built-in RF sensors can be integrated into the device to acquire local RF voltage and current measurements [5,6]. However, these take up space on the chip and can only perform measurements at one fixed location. So even though contact-based measurement techniques allow for global circuit characterisation, a method for conducting freely positionable, local RF voltage and current measurements with μm-resolution would be greatly beneficial for the development and during the prototyping phase of new RFICs.

Contactless probing techniques have been developed to measure local RF voltages. These probes often consist of an open-ended RF transmission line that ends in a sharp tip [7–11]. The tip is positioned above and perpendicular to the DUT during a measurement. The tip picks up an RF voltage through capacitive coupling. The resulting signal is transmitted to a Vector Network Analyser (VNA) where its properties are measured.

The technology of contact-less sensing of RF-voltage is closely related to scanning near-field microwave microscopy (SNMM) [12], a sub-group of the family of proximal probe microscopy with its most prominent representatives the scanning tunnelling microscope [13], and the Atomic Force Microscope (AFM) [14]. In SNMM, the near-field interaction of an active microwave-probe is used to image sample surfaces and to some extend sub-surface areas. The commonalties are in the probe that is capable of carrying a RF-signal to or from the sample or DUT resp. In the case of microscopy, the probe is active in the sense that it is the source of the RF signal, and the probe tip constitutes a sort of aperture in the wave-guiding structure whose localised near-field provides the spatial resolution for imaging. This aperture can e.g. take the form of a microfabricated co-axial tip [15]. In both cases,

* Corresponding author.
E-mail address: u.staufer@tudelft.nl (U. Staufer).

https://doi.org/10.1016/j.mne.2026.100357
Received 14 November 2025; Received in revised form 11 March 2026; Accepted 14 March 2026
Available online 31 March 2026

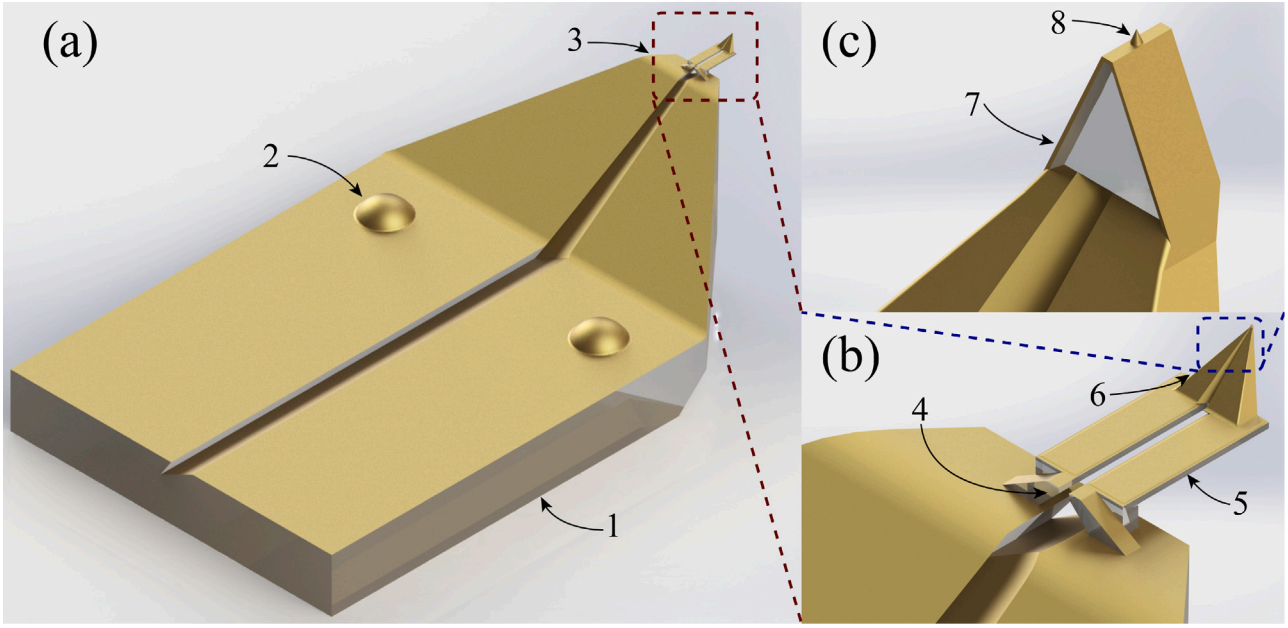

Fig. 1. Renders of the probe design with (a) an overview of the chip-body (1), showing the alignment hemispheres (2), and the build-pedestal (3). (b) shows a zoom-in of the 2PP printed structure consisting of a base (4), two-legged cantilever (5) and sensing tip (6). (c) shows a zoom-in on the sensing part of the tip, consisting of a conductive triangular loop (7) with a sharp conductive tip (8) on top.

for microscopy and RF-sensing, the probe-tip can be mounted at the end of a cantilever, in which case the technique of AFM [16,17] can be used to accurately position and move it in close proximity to the sample or DUT resp. Very briefly, the cantilever has a very high compliance such that minute forces acting on the tip deflect it. Such deflections can be measured using a laser-beam that is reflected off the cantilever and registered by a position-sensitive photo-diode. A stepper motor is approaching the probe to the sample/DUT until a certain deflection is detected, at which point a piezo-electric 3D-scanner and a servo-loop is engaged to keep the deflection signal constant while moving the probe across the sample. The servo-signal plotted versus the lateral position represents the topography of the sample. In addition, the piezo-scanner can be used to position the probe at different heights above the DUT to measure the distance dependence of the interaction force and of the RF-field produced by the DUT. Alternative to the deflection of the cantilever, its resonance frequency can be measured. In that mode of operation, a force gradient acting on the tip will change this resonance, which again can be sensed by a laser-beam and used to control the distance between the tip and the sample.

Similar to RF-voltages, local RF currents can be measured using contactless current probes [18–21]. These probes feature an electrically conductive loop with one end connected to a signal trace and the other to a ground plane. During a measurement, the loop is positioned above and parallel to a transmission line on the DUT. Inductive coupling between the DUT and the probe generates a current, which in the case of an open-loop configuration, creates a potential. The generated signal is transmitted to a VNA where it is analysed to characterise local RF current distributions in the DUT. These probes are subjected to parasitic far-field capacitive coupling between the conductive loop and the DUT. Shielding ground planes are employed to minimise these influences [18,19,21].

This limitation can be overcome with differential field probes. These make use of two parallel loops with opposite polarities [22–24]. The potential induced as a result of the current has an opposing polarity in both loops, whereas the potential induced by the voltage has a matching polarity. By analysing the potential difference between both loops local RF currents can be accurately characterised.

Recently, multi-component probes have been developed, capable of simultaneously measuring multiple signals [25–29]. Probes that allow for simultaneous RF voltage and current measurements often consist of two open-ended transmission lines that are connected through a conductive loop. During a measurement, the loop is positioned above and parallel to a transmission line on the DUT. A potential is induced in the loop, and transmitted through the RF transmission lines to a VNA. These are added to get the common-mode potential, which is used to characterise local RF voltages. Local RF currents can similarly be characterised by subtracting the measured signals from one another, to find the differential-mode potential.

Contactless probes are evaluated based on spatial resolution, sensitivity, and RF bandwidth. Designs often make trade-offs between these characteristics. Amplifying elements for example increase sensitivity, but decrease bandwidth since they only amplify signals in specific bandwidths [22,30]. Similarly, miniaturised loops and tips inherently increase the spatial resolution, but decrease the sensitivity [22].

The spatial resolution can be increased by taking several measurements at different separations between the probe and the DUT. In this method, measurements are taken at various heights and are subtracted from one another, to mitigate crosstalk of adjacent sample structures. This approach has been applied to both, RF voltage [9] and current [18] measurements. As the increments between measurements get smaller, the resolution improves, while the sensitivity decreases. To overcome this, a model-based approach has been developed [31]. Here the distance between the tip and the DUT is continuously varied during a measurement. Voltage sources directly underneath the tip will show non-linear capacitive coupling, whereas adjacent voltage sources will lead to linear capacitive coupling. By isolating the non-linear terms in the fitted model, the voltage distribution caused by voltage sources directly underneath the tip can be characterised, with μm-resolution.

This paper presents a novel multi-component probe capable of simultaneous local RF voltage and current measurements. Its intended use is the contact-less characterisation of components and building blocks of RFICs during their development and prototyping phase. It is fabricated through a multiscale 3D-printing process, followed by a thin film deposition step. The design includes a two-legged cantilever ending in a sharp sensing tip, enabling precise, AFM-based tip-circuit positioning. The design is, hence, suitable for conducting contactless RF measurements according to the model-based approach presented

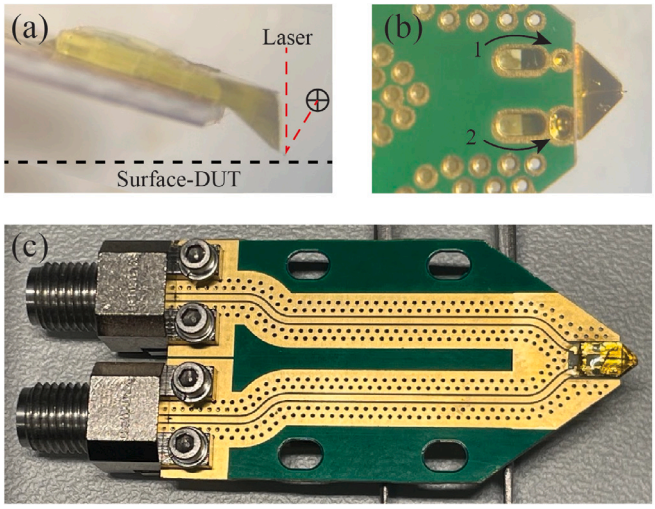

Fig. 2. Overview of a probe mounted on a PCB. (a) shows the angle of incidence with the surface of the DUT. (b) Backside of the PCB zoomed in on the alignment hole (1), and slot (2). (c) overview of the probe-PCB assembly showing connection from the probe to the transmission lines and SMA connectors.

in [31]. The model has been expanded to conduct not only contactless RF voltage measurements but also current measurements.

The paper presents the probe design in Section 2, followed by a description and model of the measurement setup in Section 3. The geometries of the fabricated probes are characterised in Section 4. In Section 5, contactless RF measurements on a microstrip are demonstrated. The conclusions of the research are presented in Section 6. Lastly, the fabrication process and measurement procedure is described in Section 7.

2. Probe description and fabrication concept

An overview of the probe geometry is shown in Fig. 1. The probe is fabricated through a multiscale 3D-printing process similar to the ones described in [32–34], followed by depositing a thin metal film on the top-side. The detailed description of the fabrication process is provided in Section 7. A chip-body, functioning as the interface between the probe and the measurement setup, is first printed by means of Digital Light Processing (DLP) stereolithography. Directly on top of this chip-body, the cantilever and the specialised tip are printed through Two-Photon Polymerisation (2PP). To facilitate an electrical connection, an electrically conductive thin Au film is deposited on top of the probe through a thermal evaporation process. To interface with the measurement setup, the probe is glued to a Printed Circuit Board (PCB) as depicted in Fig. 2c. The PCB contains two SMA connectors that transmit the measured RF signals to a VNA, where both signals are analysed to locally characterise RF voltages and currents.

2.1. Chip-body

The chip-body, depicted in Fig. 1a, functions as a mechanical and electrical interface between the PCB and the probe. It features two hemispheres that aid in aligning the probe to the PCB. To account for tolerances in the fabrication processes, the PCB includes a via hole and via slot, where the hemispheres are seated during glueing as depicted in Fig. 2b. The chip-body contains two signal paths that end in two contact pads (c.f. Fig. 1a), which were realised through the integration of a skewed-grooved separation along the middle. When the probe is glued to the PCB, the contact pads on the chip-body are pressed to the contact pads on the PCB, facilitating an electrical interface between the two.

The design freedom offered by the 3D-printing process is utilised to integrate additional functionalities into the design of the chip-body. As such, the height of the probe is increased to accommodate handling and positioning with tweezers. Furthermore, a slope is included that compensates for the thickness of the PCB. It can be seen from Fig. 2a that the probe needs to extend a certain amount to come in proximity to the DUT. By integrating a sloped extension, the probe can reach beyond the PCB. The slope features two signal paths that extend from the contact pads.

A build-pedestal for multiscale 3D-printing is placed at the top of the slope. It features the same two mutually isolated signal paths that are continued along the entire chip-body. The build-pedestal has distinct features, such as shape, and separation between the signal paths, that function as alignment markers during the subsequent 2PP steps. It can be seen from Fig. 2a that when the probe is mounted in the measurement setup, features extending past the build-pedestal still have a line of sight from above, which is a requirement for the laser read-out of the deflection of the cantilever.

2.2. Cantilever

The design includes a two-legged cantilever as depicted in Fig. 1b. It features a base, which is printed directly on top of the build-pedestal, and forms a foundation for the 2PP printed part of the probe. A slope is included in the base to create a signal path from the chip-body, to the two-legged cantilever. It includes two wide pillars that support the cantilever.

The two signal paths from the base are continued on the two-legged cantilever, leading to the sensing tip. Because the cantilever extends beyond the chip-body, a laser can be reflected of the backside, enabling deflection-measurements, like in a standard AFM-setup [17] (c.f. Fig. 2a, and Fig. 3a). To prevent the cantilever from sagging during fabrication, it is printed at an angle of 45°, with small increments of 8 μm that have an overlapping length of 4 μm. To reduce the roughness caused by the increments, a 1 μm thin layer was printed on top of the cantilever, improving the laser reflection, and signal transmission.

The two legs of the cantilever come together at the end in a square structure. This structure forms the base for the tip. The tip contains two signal paths, hence, electrical isolation between the signal paths is maintained, while the base provides mechanical stability to the tip during the subsequent fabrication steps.

2.3. Specialised tip

The tip is formed by a forward-angled square pyramid, easing the optical positioning of the tip apex during measurement. It is printed to a height of 100 μm so that it can be easily manoeuvred around obstructions, such as bond-wires. It contains another skewed-grooved separation along the middle, similar to the one applied to the chip-body, to create two mutually isolated signal paths.

A miniaturised triangular loop is situated on top of the tip, as depicted in Fig. 1c. It is made electrically conductive through the same thermal evaporation process mentioned in the beginning of Section 2, and connects the two signal paths coming from the cantilever. Small overhangs are put in place to prevent thin film deposition on the sidewalls of the loop. The structure has a constant width of 2 μm. As depicted in Fig. 4, both the base and height of the triangular structure are 5 μm long. Currents in the DUT that produce a time-varying electromagnetic flux will induce a potential over the loop, which can be analysed with the VNA to localy determine the phase and magnitude of the current.

A small plane, as depicted in Fig. 1c, is situated at the apex of the triangular loop, and a small cone is printed on top of it, using the maximum achievable resolution in our 2PP-setup. The resulting

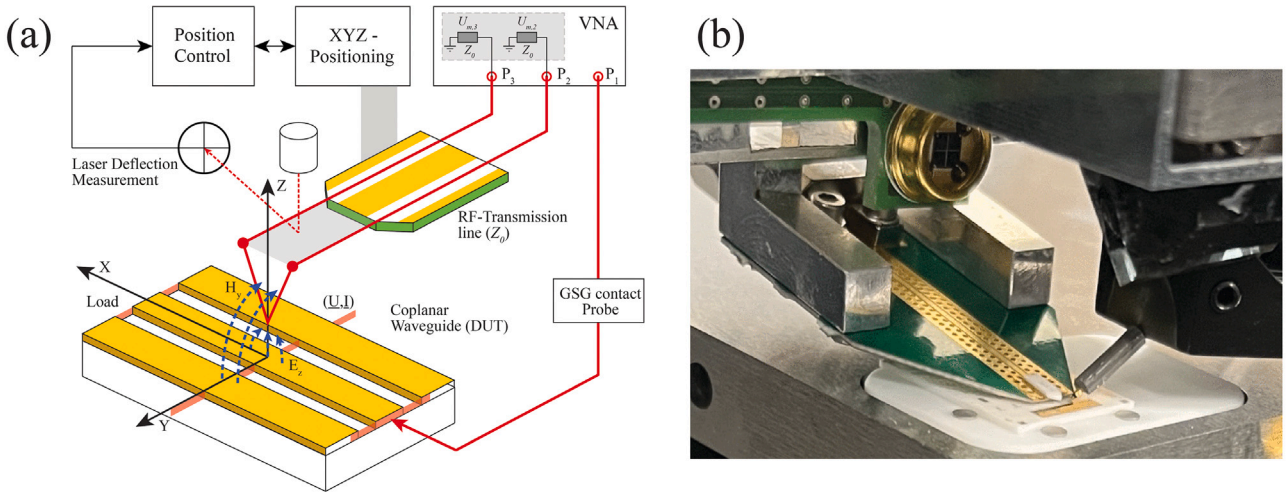

Fig. 3. (a) Schematic overview of the RF measurement setup. (b) Picture of the experimental setup, where the green PCB on the left carries the RF-probe, while the silver-grey tube coming from the black box on the right connects the Ground - Signal -Ground (GSG) contact to the coplanar waveguide.
Source: It is reprinted with permission from IEEE Sensors Journal [7].

structure as seen in Fig. 5, has an apex radius of approximately 100 nm. It acts as an open-ended transmission line, that picks up time-varying electric fields, generated by time-varying voltages. At the same time, it acts as the apex of the tip when using AFM-based positioning of the probe.

The probe design features a separate loop and tip structure. This allows for independent iteration of the functional design elements. This does however pose a trade-off. The small plane on which the conic tip is situated, acts as a parallel plate capacitor. This introduces noise during contactless voltage measurements, deteriorating the spatial resolution. The height of the conical tip can be increased to mitigate the influence of the parallel plate capacitor. This however increases the distance between the loop to the DUT resulting in a lower sensitivity during current measurements.

3. Measurement setup

The experimental setup is depicted in Fig. 3b. The probe is glued to a PCB containing two RF transmission lines with a characteristic impedance (Z_0) of 50 Ω. The PCB-probe assembly is mounted in a modified AFM-instrument, enabling the probe to be positioned above the DUT with nm-accuracy. The two signal paths originating from the PCB-probe assembly are connected to the VNA with the SMA connectors depicted in Fig. 2c. An RF signal is delivered to the DUT through a Ground-Signal-Ground (GSG) contact probe.

3.1. Tip-circuit interactions

The inductive and capacitive coupling effects can be analysed individually to locally determine the RF voltage-, and current. The local RF voltage $\underline{U}$ induces a common-mode potential $\sum \underline{U}_\mathrm{m} = \underline{U}_{\mathrm{m},2} + \underline{U}_{\mathrm{m},3}$, whereas the local RF current $\underline{I}$ is picked-up as a differential-mode potential $\Delta\underline{U}_\mathrm{m} = \underline{U}_{\mathrm{m},2} - \underline{U}_{\mathrm{m},3}$. The capacitive coupling can be modelled as the tip-circuit capacitance C in series with two parallel transmission lines. Whereas the inductive coupling is modelled as the tip-circuit inductance L, in series with the loop, which in turn is in series with two parallel transmission lines. The resulting relations are described by the equations below [7]:

$$\sum \underline{U}_\mathrm{m} = \underline{U} \cdot \frac{j\omega 2 Z_0 C}{2 + j\omega Z_0 C} \approx \underline{U} \cdot j\omega Z_0 C \tag{1}$$

$$\Delta\underline{U}_\mathrm{m} = \underline{I} \cdot \frac{j\omega 2 Z_0 L}{2Z_0 + Z_l} \approx \underline{I} \cdot j\omega L \tag{2}$$

The simplifications made in Eqs. (1) & (2) are only valid as long as $C \ll \frac{2}{\omega Z_0}$ and $Z_l \ll 2Z_0$. Where the variables ω, Z_l, and $Z_0 = 50\,\Omega$ denote the angular frequency, the impedance of the loop, and the impedance of the transmission lines respectively. These assumptions hold for frequencies $\omega < 26$ GHz, and the proposed probe geometry and setup.

3.2. Model-based measurement approach

The model-based approach as presented in [7], provides a method to eliminate parasitic far-field cross-talk by performing continuous voltage measurements while varying the vertical tip-circuit distance. The total capacitance C [35] and inductance L between the probe and the circuit, are both dependent on the tip-circuit distance z. They can be subdivided in short-range nonlinear components that originate from electrodes right underneath the tip, and long-range approximately linear components that are due to parasitic sources originating further away from the tip. The following equations mathematically depict these effects:

$$C(z) = \underbrace{C_\mathrm{nl}(z)}_{\text{short-range}} + \underbrace{C_\mathrm{lin}(z)}_{\text{long-range}} \tag{3}$$

$$L(z) = \underbrace{L_\mathrm{nl}(z)}_{\text{short-range}} + \underbrace{L_\mathrm{lin}(z)}_{\text{long-range}} \tag{4}$$

The nonlinear component of the capacitance $C_\mathrm{nl}(z)$ can be described by a logarithmic dependency on the tip-circuit distance [7,35]. Similarly, the inductance $L_\mathrm{nl}(z)$ follows an inverse dependence on the tip-circuit distance. These relations are described by the following equations:

$$C_\mathrm{nl}(z) = C_0 \cdot \ln\left(1 + \frac{R_\mathrm{eff}}{z}\right) \tag{5}$$

$$L_\mathrm{nl}(z) = L_0 \cdot \left(1 + \frac{A_\mathrm{eff}}{z}\right) \tag{6}$$

Where C_0 and L_0 represent a constant capacitance, and inductance. The terms R_eff and A_eff denote the effective tip-apex radius and the effective area enclosed by the loop, which account for the shape and size of the tip. It is evident from Eqs. (5) & (6) that especially for small tip-circuit distances z, on the order of R_eff and A_eff, the nonlinear components become significant. Parasitic coupling between the probe and circuit parts at larger distances, however, follow linear dependencies, described by $C_\mathrm{lin} = a \cdot z + b$, and $L_\mathrm{lin} = c \cdot z + d$. As

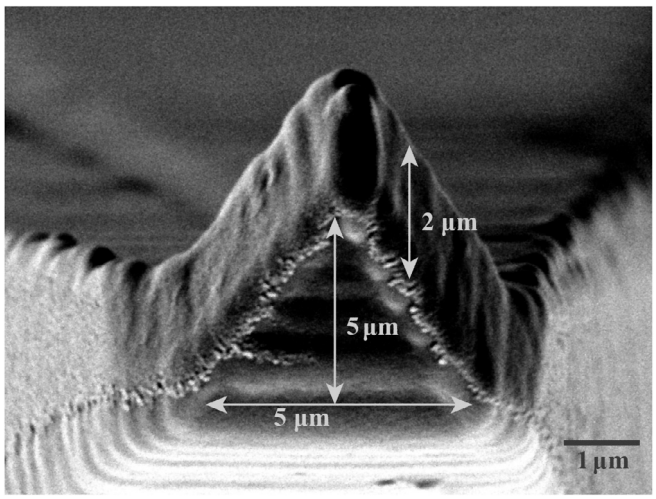

Fig. 4. SEM image of the hybrid tip containing the dimensions of the miniaturised loop.

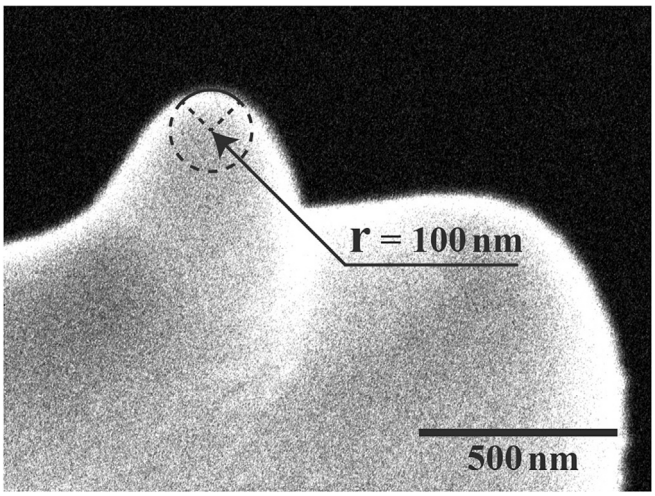

Fig. 5. SEM image of the electrically-conductive miniaturised tip showing the apex radius of the tip.

such, the signals measured by the VNA according to Eqs. (1) & (2), can also be subdivided into a long-, and short-range component.

$$\sum \underline{U}_{\mathrm{m}}(z) \propto \underbrace{\underline{U} \cdot C_{\mathrm{nl}}(z)}_{\text{short-range}} + \underbrace{\underline{U}_{\mathrm{lin}} \cdot C_{\mathrm{lin}}(z)}_{\text{long-range}} \tag{7}$$

$$\Delta\underline{U}_{\mathrm{m}}(z) \propto \underbrace{\underline{I} \cdot L_{\mathrm{nl}}(z)}_{\text{short-range}} + \underbrace{\underline{I}_{\mathrm{lin}} \cdot L_{\mathrm{lin}}(z)}_{\text{long-range}} \tag{8}$$

The local short-range coupling terms are represented by $C_{\mathrm{nl}}(z)$, and $L_{\mathrm{nl}}(z)$. Looking back at Eqs. (5) & (6), it is presumed that the non-linear coupling terms are significant only for circuit parts close to the tip. Hence, the non-linear coupling terms correspond only to local RF voltages $\underline{U}$ [7] and currents $\underline{I}$. The remaining parasitic coupling effects between circuit elements and the probe follow a linear dependency on the tip-circuit distance, and are therefore all represented into a combined long-range voltage $\underline{U}_{\mathrm{lin}}$ [7] and current $\underline{I}_{\mathrm{lin}}$.

By identifying the local RF voltage $\underline{U}$ and current $\underline{I}$, from equations Eqs. (7) & (8), parasitic contributions captured in $\underline{U}_{\mathrm{lin}}$, and $\underline{I}_{\mathrm{lin}}$ can be eliminated. As the tip-circuit distance is continuously increased during a measurement, a complex fit can be decomposed to identify the magnitude and phase of both the linear, and non-linear components. As such, both the magnitude and phase of local RF voltage $\underline{U}$ and current $\underline{I}$ can be identified.

4. Probe characterisation

In order to corroborate the novel fabrication process for the application of contactless RF voltage and current probes, a Scanning Electron Microscope (SEM) (JSM-6010LA, JEOL Ltd., Japan) has been employed. It allows for geometrical inspection with nm-resolution, making it suitable for determining the tip apex radius, and the dimensions of the conductive loop. As shown earlier in Eqs. (5) & (6), these dimensions play an important role in predicting the spatial resolution.

4.1. Functional design elements

As mentioned, the area enclosed by the conductive loop, and the tip apex radius of the sharp conductive tip, determine the spatial resolution that can be achieved with the probe. Hence, a SEM inspection has been conducted to verify these dimensions, and thus estimate the spatial resolution that can be achieved with the probe. The electrical isolation resulting from the skewed-grooved separations has been verified experimentally with a 4-point probe. For this experiment, a plain chip-body without cantilever and tip was used. In this configuration, a current could be detected between the alignment hemisphere and build-pedestal. In contrast, no current could be detected between the 2 alignment hemispheres as a result of the skewed-groove.

The sharp conductive tip as shown in Fig. 5 has a tip apex radius of approximately 100 nm, which is similar to the tip apex radius used in [31], resulting in an effective tip apex radius of $R_{\mathrm{eff}} \approx 1\,\mu\mathrm{m}$. According to Eq. (5) this allows for measurements with µm-resolution. However, the tip sits on a small plane, which will act as a parallel plate capacitor, deteriorating the spatial resolution.

The dimensions of the triangular conductive loop as depicted in Fig. 4 show the dimensions where the base and height are both equal to 5 µm, hence, the loop encloses an area of 12.5 $\mu\mathrm{m}^2$, where the loop has a constant width of 2 µm.

4.2. Inductive coupling simulations

The spatial resolution that can be achieved with the loop dimensions has been evaluated with simulations that do not employ the model-based approach, so that the probe fabrication method can be compared to conventional techniques. The method of determining the spatial resolution as presented in [26] has been employed. In the simulations, the tip-circuit distance is kept constant while the probe is moved over a cross-section of a Microstrip that functions as the DUT. The spatial resolution is determined as the coordinate where the normalised signal crosses the −6 dB threshold. Adjusting the DUT and tip-circuit distance influences this value. With the probing setup presented in Fig. 3, tip-circuit distances as small as 100 nm can be achieved. As can be seen from Fig. 6, it is estimated from simulations that at this tip-circuit distance, a spatial resolution of 3 µm can be expected.

5. Contactless RF measurements on a transmission line

To demonstrate the effectiveness of the newly designed RF-probe, we executed multiple measurements using a single probe on an open-ended microstrip transmission line, that acted as the DUT. As the open-end will have an impedance mismatch it is assumed that the signal is fully reflected, leading to standing waves. The microstrip comprises a 2 µm-wide conductor, that is fully encapsulated by a passivation layer with a relative permittivity $\varepsilon_r = 4.0$. The thickness of the passivation layer above the conductor is 2 µm. Its surface was planarised. The tip-circuit distance z is measured from this surface to the tip apex. By applying the model-based approach to a measurement over a cross-section of the microstrip the spatial resolution of the probe can be

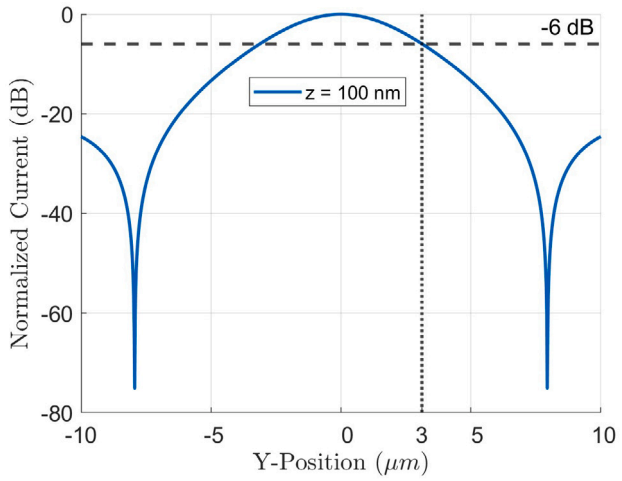

Fig. 6. Cross-sectional current simulation, at a tip-sample distance of z = 100 nm, showing a simulated spatial resolution of approximately 3 µm.

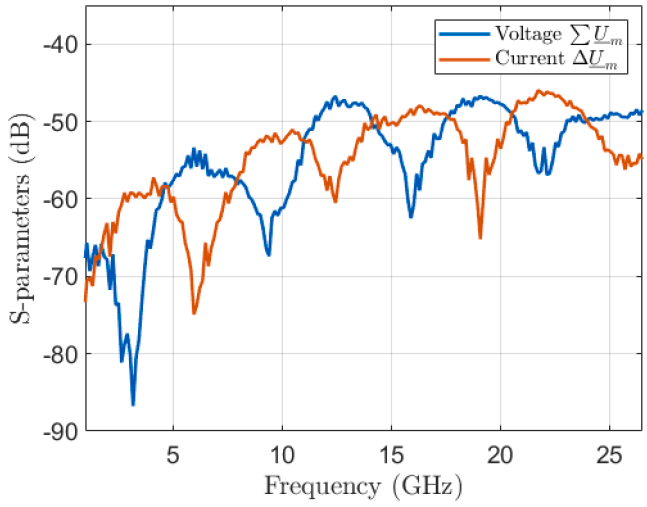

Fig. 7. A contactless RF voltage, and current measurement where the probe is kept at a fixed position, approximately 10 µm above the DUT.

evaluated. Next to that, the probe can be positioned at a fixed location above the microstrip while the frequency is swept to evaluate the measurement bandwidth.

5.1. Stationary contactless measurement

A second measurement is performed where the probe is kept above the microstrip at a fixed tip-circuit distance of approximately 10 µm. The frequency of the signal supplied to the microstrip is continuously increased from 1 to 26.5 GHz, while both the common-mode-, and differential mode potential are measured. It is expected from Eqs. (1) & (2) that both the common-mode and differential-mode potential show a linear increase with frequency. Due to the standing waves resulting from the reflections at the open-ended transmission line, the voltage and current will increase with frequency showing alternating polarities. Hence, the graphs represented in Fig. 7 confirm that the common-mode, and differential-mode potential represent the RF voltage and current respectively.

It is assumed that the bandwidth of the probe is limited by reflected signals due to an impedance mismatch at the interface between the probe and the PCB. When the length between this interface and the

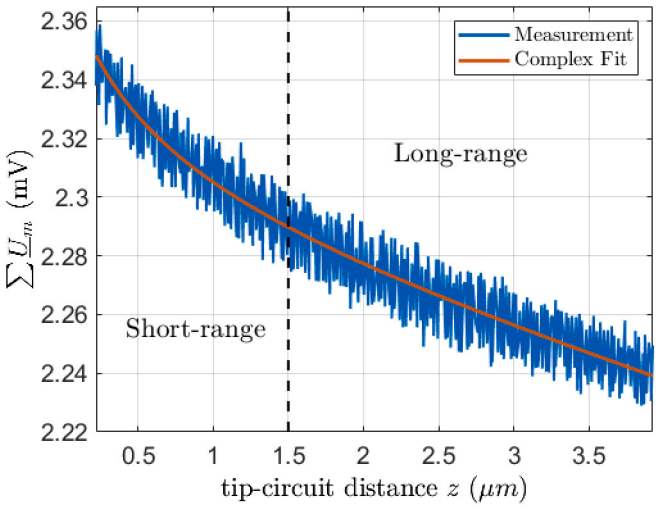

Fig. 8. Model-based complex fitting to a common-mode potential vs. tip-circuit distance measurement, where there can be distinguished between short-, and long-range distance dependencies.

probe-tip approaches the quarter wavelength ($\lambda/4$) of the measured signal, reflections will become more significant. Therefore minimising the length of the signal path will result in a larger bandwidth [7]. When the signal path has a length equal to $\lambda/4$, an anti-resonance will be observed, as the probe will act as a quarter wavelength attenuator. The length of the signal path lies in the range of 5 mm to 2 mm, as the exact location where the signal passes through the contact pads that form the probe-PCB interface is unclear. The highest measurement frequency that can be achieved with this probe therefore lies between 15 and 37.5 GHz. At a frequency of 23 GHz curve flattening can be made out from the voltage measurement. The contactless RF probe therefore has a characterised measurement bandwidth ranging from 1 to 23 GHz.

5.2. Cross-sectional measurement

The model-based approach as earlier described in Section 3.2 is applied to conduct several measurements along the Y-coordinate as indicated in Fig. 3 to assess the spatial resolution of the probe. In order to apply the model-based approach a short-range nonlinear tip-circuit distance dependency needs to be distinguishable. In Fig. 8 such a $\sum \underline{U}_{\mathrm{m}}$ versus tip-circuit distance measurement is shown, where the data is used to perform a complex fit. It can be seen that the short-range signal ($z < 1.5$ µm) contains a non-linear component, whereas the long-range signal is dominated by an approximately linear tip-circuit distance dependency. Performing these fitting procedures has been successful for contactless RF voltage measurements. The spatially distributed measurements a cross the microstrip, are depicted in Fig. 9. From here, the spatial-resolution of the probe when used as RF-voltage sensor can be evaluated. As there is no standardised method to determine the spatial-resolution, we define it as the distance between the two points, where the normalised signal crosses the −6 dB threshold. The spatial-resolution is therefore approximately 8 µm.

Unfortunately, we failed to conduct the corresponding measurements for RF-currents because of probe-failures. For such a measurement, the tip is positioned above the DUT, then lowered to the surface until it gently touches it. This mechanical contact with the passivation layer defines the origin of the z-axis. The tip is then pulled back while recording the RF-current signal. This movement of the tip is the same as the one executed for 'force-distance curve' measurements in an AFM. It was done with a repetition rate of 1 Hz. We speculate that we accidentally touched the DUT too hard even though the AFM-based approach should prevent destructive interactions. Alternatively,

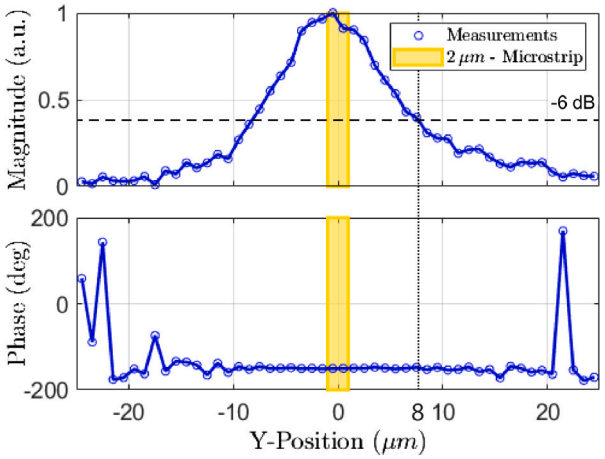

Fig. 9. Contactless RF voltage measurement at a frequency of 10 GHz according to the model-based approach [7] over a cross-section of a 2 µm wide microstrip.

the miniaturised loop could also have been destroyed due to electrical discharge. Both explanations remain speculative as no SEM analyses of the tip was made after use.

6. Conclusion

In this paper the model-based approach presented in [7] has been expanded to conduct both contactless local RF voltage and current measurements. A corresponding probe is manufactured in a novel fabrication process for the application of multicomponent near-field probes, or contactless RF voltage and current probes. It resulted in a sharp conductive tip with a tip apex radius of 100 nm, that sits on top of a miniaturised triangular conductive loop that encloses an area of 12.5 µm^2. The simulated spatial resolution for contactless RF current measurements according to the criteria presented in [26] was calculated to be 3 µm.

Using one of these probes, the basic functionality was demonstrated. This was done by first determining the bandwidth of the probe by conducting a stationary, contactless RF-voltage and RF-current measurement. For that purpose, the probe was positioned 10 µm above the microstrip, while the signal frequency on the DUT was increased. Both the common-mode potential representing the RF-voltage signal, and differential-mode potential representing the RF-current signal were measured as depicted in Fig. 7. Curve flattening, indicative for bandwidth limitation, was observed with contactless voltage measurements at frequencies above 23 GHz. With these preliminary results we could demonstrate the basic operability of our probe and the successful implementation of the fabrication process. The probe can be employed for contactless RF voltage and current measurements that lie in a bandwidth of 1 to 23 GHz.

A model-based approach has been applied to contactless RF voltage measurements over a cross-section of a Microstrip, with which a spatial resolution of 8 µm was experimentally determined according to the method provided in [26]. The achieved spatial resolution in RF-voltage measurements is about five to ten times worse than what was achieved in earlier work [31], where interdigitated metal combs could be resolved, to which resp. an RF-signal and ground was applied, and which had dimensions of 2 µm lines and 1.6 µm spaces. The experimental set-up was comparable to ours, except that the probe comprised a single, slender metal (Pt) tip of 80 µm in length, placed at the end of a 300 µm long and 110 µm wide metallic cantilever. The tip radius was less than 2 nm. In our case, we used a blunter, 100 nm radius, and shorter tip of about 1 µm length, which was positioned on a plane of about 2 µm by 0.5 µm that terminates the current-sensing loop. We assume that primarily this relatively large plane close to the tip apex negatively affects the spatial resolution of RF-voltage measurements. This is supported by the measured common-mode potential versus tip - circuit distance (Fig. 7), where we observed that non-linear effects extend to more than 1 µm. While increasing the tip length and hence the spatial resolution would be possible, it would position the current-sensing loop further away from the device and, hence, deteriorate the spatial resolution of current measurements. An optimised length must still be found and will be part of future developments.

The probes are very delicate to handle, both in terms of mechanical robustness of the tip and electrostatic-discharge sensitivity. An inadvertent contact between DUT and probe may destroy the tip and/or the loop. Such probe failure prevented us from experimentally verifying the simulated spatial resolution of 3 µm for RF-current measurements.

In future industrial applications of our probe, signals between components or functional building blocks of a RF-IC shall be measured during the development and prototyping phase. Such components are connected via metal lines, which have typical widths of a few micrometre and a thickness of up to a few hundred nanometre. These interconnects are typically integrated in the last metal layer at the surface of the device, and they are encapsulated with a passivation layer of 1–2 µm in thickness. The intermetal layer is normally planarised prior to the deposition of the passivation layer, hence, topographic variations are expected to be small, and the dimensions of the configuration are comparable to the microstrip that we used as test-sample, and which we therefore consider as representative for real devices.

It might be preferred, that during the development phase the passivation layer is reduced to 100 nm such that the probe can pick up more of the near-field of the interconnect making the suppression of cross-talk from near-by elements by the model-based approach more effective (c.f. also Fig. 8). Nonetheless, the expected topographical variations in the vicinity of where the signals shall be assessed in a real-word-application are such that our RF-probe (Fig. 1c and Fig. 5) can be placed without hindrance. The roughness of the passivation layer after planarisation is typically less than 10 nm. Therefore, a line profile across a connection can be performed using AFM-based techniques. Possible remaining obstacles are bond wires or probes that connect the DUT. These are addressed by the forward-inclined square pyramid of 100 µm height (c.f. Fig. 1b) which carries the proper probe. In addition, the entire probe and the PCB onto which it is mounted are inclined by about 10° to the surface of the DUT (c.f. Fig. 3b). Still, placement of the probe is critical and certain azimuthal angles might be inaccessible.

7. Methods

In this section, the fabrication process is presented, in which a multiscale 3D-printing approach has been optimised in combination with a thermal evaporation process in order to fabricate probes capable of contactless RF voltage and current measurements. The measurement procedure for performing contactless model-based RF voltage [7] and current measurements is also discussed.

7.1. Fabrication process

As mentioned before in Section 2 a multiscale 3D-printing process is used to fabricate the probe substrate. The chip body is printed with a DLP-printer (Micro2, microSLA, USA) in combination with a compatible high-resolution resin (UHR, microSLA, USA). The step height in the Z-direction is set to 1 µm, while the XY-resolution is set to 5 µm. The prints are cleaned in IPA (99.8 % Honeywell, Riedel-de-Haën, Germany) in two subsequent steps of 2 min each.

To align the chip-bodies in the 2PP setup, a chip-body holder is 3D-printed in a DLP-printer (Micro Plus HiRes, EnvisionTEC GmbH, Germany) with an XYZ-resolution of 35 µm, using a proprietary photoresist (HTM140v2, EnvisionTEC GmbH, Germany). The resulting structure

Table 1
Printing parameters used in the 2PP process.

	Base	Cantilever	Sensing Tip
Laser power[a]	40 %	50 %	30 %
Scanning speed ($mm\,s^{-1}$)	10	40	7
Slicing distance (μm)	0.3	0.2	0.1
Hatching distance (μm)	0.3	0.2	0.1
Galvo acceleration ($V\,ms^{-2}$)	5	5	1

[a] Given as the percentage of the total laser power of 50 mW.

including supports is cleaned in an ultrasonic cleaner using IPA (99.8 % Honeywell, Riedel-de-Haën, Germany) before post-exposure curing it in a UV-oven at 80 °C in combination with UV-light for 20 min. During the curing step, it is clamped between two microscope-slides. Lastly, the 3D-printing supports are removed.

The chip-bodies are placed in the 3D-printed chip-body holder, which are sub-sequentially loaded into a designated 9 × 9 sample holder. Prior to loading the 9 × 9 holder into the 2PP-setup (Photonic Professional GT Laser Lithography System, Nanoscribe GmbH, Germany), a high-resolution negative tone resin (IP-Dip, Nanoscribe GmbH, Germany) is dispensed on the chip-bodies at the desired printing locations. The 2PP printing-process is optimised for each distinct part as noted in Table 1. At the start of the printing process, the interface of the chip-body is manually identified, and the laser of the 2PP system focused approximately 5 μm below the surface of the chip-body. All parts are printed in the so-called 63x magnification DiLL configuration. The samples are developed in two steps. In the first step, they are submerged for 5 min in propylene-glycol-methyl-ether-acetate (PGMEA, Sigma– Aldrich, USA), and subsequentially another 20 min in IPA (99.8 % Honeywell, Riedel-de-Haën, Germany).

For the next fabrication step, the metalization of the front-side, the probes are mounted in a thermal evaporator (Temescal FC-2000, Ferrotec USA, USA). To deposit a Titanium (Ti) adhesion layer of 10 nm, the chamber is first evacuated to a pressure of 2 mTorr. While the sample holder is rotating at a speed of 10 RPM, the material is deposited with a deposition rate of $0.5\,Å\,s^{-1}$. In the subsequent deposition step, a 100 nm Gold (Au) thin film is deposited at a pressure of 3 mTorr. The sample holder again rotates with 10 RPM, while the deposition rate is kept at $1.0\,Å\,s^{-1}$.

During the development phase, different elements of the probe and several design variants were fabricated (results not shown). A total of 25 probes were finally processed and one batch of 5 probes of one design variant was selected for testing its suitability for RF-voltage and -current measurements. Handling the probes is critical, and has to follow Electrostatic Discharge (ESD)-rules. In the final assembly step, the probes are carefully aligned to the PCBs with the assistance of the previously mentioned alignment hemispheres. The sides of the probes are then glued (Loctite 401, Henkel AG & Co. KGaA, Germany) to the PCB, yielding the final probe-PCB assembly.

7.2. Measurement procedure

The measurement procedure is similar to the one presented in [7]. The PCB-probe assembly is first mounted in the modified AFM-instrument. The focus of the read-out laser is then aligned to the end of the cantilever, so that the signal of the reflected beam on the photodiode is maximised. Using this laser read-out is essential to control the relative height of the probe above the DUT by exploiting the technique of AFM. The SMA-connectors on the PCB-probe assembly, and GSG contact probe, now need to be connected to the VNA.

An optical microscope and stepper motors are used for the alignment in XY-directions, and to approach the surface of the circuit to the probe. The more accurate vertical piezo is actuated to identify the surface of the DUT, such that the probe approaches the circuit with constant velocity. As the probe makes mechanical contact the cantilever deflects, which is detected by the photodiode, and the approaching motion is stopped. For the contactless measurements, only distances $z > 100$ nm (see Fig. 3a for the orientation of the z-axis) above the surface are considered, hence, contactless (i.e. without electrical contact between DUT and probe) RF measurements can be performed.

During a RF-measurement, the DUT receives a signal from the VNA through the GSG contact probe. The RF probe is then positioned above (i.e. z>0) the DUT at a desired XY-coordinate. Both the common-mode potential, and the differential-mode potential are continuously measured while the tip-circuit distance is increased. To eliminate parasitic contributions to the signal, the model-based approach as presented in Section 3.2 can be applied to identify the local RF voltage $\underline{U}$ and current $\underline{I}$. This procedure is repeated e.g. for each y-coordinate of cross-sectional measurements like the one shown in Fig. 9.

CRediT authorship contribution statement

Maarten Jankie: Developed, fabricated and characterized the probes. **Thomas Hackl:** conducted and analyzed the RF measurements. **Georg Schitter:** Conceived and supervised the project. **Urs Staufer:** Conceived and supervised the project.

Declaration of competing interest

The authors declare the following financial interests/personal relationships which may be considered as potential competing interests: Given his role as associated Editor of the MNE Journal, U. Staufer declares that he had no involvement in the peer review of this article and had no access to information regarding its peer review. Full responsibility for the editorial process for this article was delegated to another journal editor. If there are other authors, they declare that they have no known competing financial interests or personal relationships that could have appeared to influence the work reported in this paper.

Acknowledgements

We thank M. Poik (TU Vienna) for valuable discussions in the beginning of the project, and A. Bogard and the team of technicians at TU Delft for their support during the fabrication of the probes.

Data availability

Data will be made available on request.

References

[1] Y.-C. Chang, P.-Y. Wang, D.-C. Chang, S.-S. Hsu, A low-loss fully integrated CMOS active probe for gigahertz conducted EMI test, IEEE Trans. Microw. Theory Tech. 67 (4) (2019) 1652–1660, http://dx.doi.org/10.1109/TMTT.2019.2897926.

[2] M. Poik, T. Hackl, S. Di Martino, M. Schober, J. Dang, G. Schitter, Analysis of cross-talk induced measurement errors in model-based RF voltage sensing, in: 2023 IEEE International Instrumentation and Measurement Technology Conference (I2MTC), 2023, pp. 1–6, http://dx.doi.org/10.1109/I2MTC53148.2023.10175924.

[3] A. Rumiantsev, R. Doerner, RF probe technology: History and selected topics, IEEE Microw. Mag. 14 (7) (2013) 46–58, http://dx.doi.org/10.1109/MMM.2013.2280241.

[4] V. Solomko, O. Özdamar, R. Weigel, A. Hagelauer, Model of substrate capacitance of MOSFET RF switch inspired by inverted microstrip line, in: 51st IEEE European Solid-State Device Research Conference, ESSDERC, IEEE, Grenoble, France, 2021, pp. 207–210, http://dx.doi.org/10.1109/ESSDERC53440.2021.9631806.

[5] S. Ziegler, R.C. Woodward, H.H.-C. Iu, L.J. Borle, Current sensing techniques: A review, IEEE Sensors J. 9 (4) (2009) 354–376, http://dx.doi.org/10.1109/JSEN.2009.2013914.

[6] O. Özdamar, A.M. Hagelauer, R. Weigel, V. Solomko, An RF voltage detector with low harmonic feedback for antenna tuning switches, in: 2019 IEEE International Conference on Microwaves, Antennas, Communications and Electronic Systems, COMCAS, IEEE, Tel-Aviv, Israel, 2019, pp. 1–5, http://dx.doi.org/10.1109/COMCAS44984.2019.8958276.

[7] M. Poik, T. Hackl, S. Di Martino, B.M. Berger, S.W. Sattler, G. Schitter, A contactless method for measuring amplitude and phase of RF voltages up to 26.5GHz, IEEE Sensors J. (2024) http://dx.doi.org/10.1109/JSEN.2024.3354322.

[8] W. Fang, H. Qiu, C. Luo, L. Wang, E. Shao, Noncontact RF voltage sensing of a printed trace via a capacitive-coupled probe, IEEE Sensors J. 18 (21) (2018) 8873–8882, http://dx.doi.org/10.1109/JSEN.2018.2869908.

[9] R. Kantor, I.V. Shvets, Measurement of electric-field intensities using scanning near-field microwave microscopy, IEEE Trans. Microw. Theory Tech. 51 (11) (2003) 2228–2234, http://dx.doi.org/10.1109/TMTT.2003.818938.

[10] R. Hou, M. Spirito, R. Heeres, F. van Rijs, L.C.N. de Vreede, Non-intrusive near-field characterization of distributed effects in large-periphery LDMOS RF power transistors, in: 2015 IEEE MTT-S International Microwave Symposium (IMS), IEEE, 2015, pp. 1–3, http://dx.doi.org/10.1109/MWSYM.2015.7166945.

[11] N. Dehghan, S.C. Cripps, A novel in-situ calibration technique for a high resolution E-field probe, in: 2015 IEEE MTT-S International Microwave Symposium, IMS, IEEE, Phoenix, AZ, USA, 2015, pp. 1–3, http://dx.doi.org/10.1109/MWSYM.2015.7166745.

[12] B.T. Rosner, D.W. van der Weide, High-frequency near-field microscopy, Rev. Sci. Instrum. 73 (7) (2002) 2505–2525, http://dx.doi.org/10.1063/1.1482150.

[13] G. Binnig, H. Rohrer, C. Gerber, E. Weibel, Surface studies by scanning tunneling microscopy, Phys. Rev. Lett. 49 (1) (1982) 57–61, http://dx.doi.org/10.1103/PhysRevLett.49.57.

[14] G. Binnig, C.F. Quate, C. Gerber, Atomic force microscope, Phys. Rev. Lett. 56 (9) (1986) 930–933, http://dx.doi.org/10.1103/PhysRevLett.56.930.

[15] M. Tabib-Azar, Y. Wang, Design and fabrication of scanning near-field microwave probes compatible with atomic force microscopy to image embedded nanostructures, IEEE Trans. Microw. Theory Tech. 52 (3) (2004) 971–979, http://dx.doi.org/10.1109/TMTT.2004.823596.

[16] F.J. Giessibl, C.F. Quate, Exploring the nanoworld with atomic force microscopy, Phys. Today 59 (12) (2006) 44–50, http://dx.doi.org/10.1063/1.2435681.

[17] O.H. Olubowale, S. Biswas, G. Azom, B.L. Prather, S.D. Owoso, K.C. Rinee, K. Marroquin, K.A. Gates, M.B. Chambers, A. Xu, J.C. Garno, “May the force be with you!" force-volume mapping with atomic force microscopy, ACS Omega 6 (40) (2021) 25860–25875, http://dx.doi.org/10.1021/acsomega.1c03829.

[18] Y.T. Chou, H.C. Lu, Space difference magnetic near-field probe with spatial resolution improvement, IEEE Trans. Microw. Theory Tech. 61 (12) (2013) 4233–4244, http://dx.doi.org/10.1109/TMTT.2013.2288089.

[19] Z. Yan, W. Liu, J. Wang, D. Su, X. Yan, J. Fan, Noncontact wideband current probes with high sensitivity and spatial resolution for noise location on PCB, IEEE Trans. Instrum. Meas. 67 (12) (2018) 2881–2891, http://dx.doi.org/10.1109/TIM.2018.2830859.

[20] H. Qiu, W. Fang, Y. En, Y. Huang, Y. Liu, P. Lai, Y. Chen, C. Shi, Movable noncontact RF current measurement on a PCB trace, IEEE Trans. Instrum. Meas. 66 (9) (2017) 2464–2473, http://dx.doi.org/10.1109/TIM.2017.2698900.

[21] N. Ando, N. Masuda, N. Tamaki, T. Kuriyama, K. Kato, M. Saito, S. Saito, K. Ohashi, M. Yamaguchi, Miniaturized Thin-film Magnetic Field Probe with High Spatial Resolution for LSI Chip Measurement, Tech. rep., New Industry Creation Hatchery Center (NICHe), Tohoku University, 2004.

[22] J. Wang, Z. Yan, J. Liu, Y. Zhou, C. Fu, D. Su, Miniature active differential magnetic field probe with high sensitivity for near-field measurements, IEEE Trans. Antennas and Propagation 70 (2) (2022) 1575–1580, http://dx.doi.org/10.1109/TAP.2021.3111300.

[23] W. Shao, Y. Chen, L. Huang, W. Fang, An asymmetric correction method for differential double-loop magnetic field probing system, IEEE Trans. Antennas and Propagation 71 (10) (2023) 6349–6354, http://dx.doi.org/10.1109/TAP.2023.3299050.

[24] G. Li, W. Shao, R. Chen, Y. Zhang, Z. Wang, Ultrawideband differential magnetic near field probe with high electric field suppression, IEEE Sensors J. 20 (14) (2020) 7669–7676, http://dx.doi.org/10.1109/JSEN.2020.2981764.

[25] R. Yang, X.-C. Wei, Y.-F. Shu, D. Yi, Y.-B. Yang, A miniature multi-component probe for near-field scanning, IEEE Trans. Antennas and Propagation 67 (11) (2019) 6821–6828, http://dx.doi.org/10.1109/TAP.2019.2927814.

[26] L. Wang, X. Liu, W. Shao, Z. Zhu, An ultrawideband four-port composite probe with simultaneous measurement of multicomponent fields and improvement of electric-field suppression, IEEE Trans. Components, Packag. Manuf. Technol. 13 (8) (2023) 1278–1286, http://dx.doi.org/10.1109/TCPMT.2023.3299981.

[27] W. Shao, W. Fang, Y. Huang, Z. Liu, X. Dong, Simultaneous measurement of electric and magnetic fields with a dual probe for efficient near-field scanning, IEEE Trans. Antennas and Propagation 67 (4) (2019) 2859–2864, http://dx.doi.org/10.1109/TAP.2019.2897476.

[28] C. Luo, W. Fang, Y. Shen, H. Qiu, F. Yu, H. Li, Collocated and simultaneous measurements of RF current and voltage on a trace in a noncontact manner, IEEE Trans. Microw. Theory Tech. 67 (6) (2019) 2406–2415, http://dx.doi.org/10.1109/TMTT.2019.2905204.

[29] W. Shao, Z. Yi, X. He, W. Fang, C. Zhou, J. Liu, Novel calibration method for the asymmetric probing in the near-field measurement with a dual probe, IEEE Trans. Microw. Theory Tech. 69 (12) (2021) 5439–5448, http://dx.doi.org/10.1109/TMTT.2021.3120140.

[30] W. Shao, J. Li, Q. Huang, E. Shao, J. Liu, A two-turn loop active magnetic field probe design for high sensitivity near-field measurement, IET Sci. Meas. Technol. 16 (1) (2022) 40–49, http://dx.doi.org/10.1049/smt2.12083.

[31] M. Poik, T. Hackl, S. Di Martino, M. Schober, J. Dang, G. Schitter, Model-based RF sensing for contactless high-resolution voltage measurements, IEEE Trans. Instrum. Meas. 72 (2023) 1–8, http://dx.doi.org/10.1109/TIM.2023.3317385.

[32] M. Blankespoor, T. Manzaneque, M.K. Ghatkesar, Discrete femtolitre pipetting with 3D printed axisymmetrical phaseguides, Small Methods 8 (3) (2024) 2300942, http://dx.doi.org/10.1002/smtd.202300942.

[33] R.C. Kramer, E.J. Verlinden, L. Angeloni, A. van den Heuvel, L.E. Fratila-Apachitei, S.M. van der Maarel, M.K. Ghatkesar, Multiscale 3D-printing of microfluidic AFM cantilevers, Lab A Chip 20 (2) (2020) 311–319, http://dx.doi.org/10.1039/C9LC00668K.

[34] P.F.J. van Altena, Multiscale 3D Printed Polymer Probes for Single Cell Experiments, (Master’s thesis), TU Delft, 2021.

[35] L. Fumagalli, G. Ferrari, M. Sampietro, I. Casuso, E. Martinez, J. Samitier, G. Gomila, Nanoscale capacitance imaging with attofarad resolution using ac current sensing atomic force microscopy, Nanotechnology 17 (18) (2006) 4581–4587, http://dx.doi.org/10.1088/0957-4484/17/18/009.